

Northumbria Research Link

Citation: Kang, Zhe, Yuan, Jinhui, Zhang, Xianting, Wu, Qiang, Sang, Xinzhu, Farrell, Gerald, Yu, Chongxiu, Li, Feng, Tam, Hwa Yaw and Wai, Ping-kong Alexander (2014) CMOS-compatible 2-bit optical spectral quantization scheme using a silicon-nanocrystal-based horizontal slot waveguide. Scientific Reports, 4. p. 7177. ISSN 2045-2322

Published by: Nature Publishing

URL: <https://doi.org/10.1038/srep07177> <<https://doi.org/10.1038/srep07177>>

This version was downloaded from Northumbria Research Link:
<http://nrl.northumbria.ac.uk/id/eprint/22442/>

Northumbria University has developed Northumbria Research Link (NRL) to enable users to access the University's research output. Copyright © and moral rights for items on NRL are retained by the individual author(s) and/or other copyright owners. Single copies of full items can be reproduced, displayed or performed, and given to third parties in any format or medium for personal research or study, educational, or not-for-profit purposes without prior permission or charge, provided the authors, title and full bibliographic details are given, as well as a hyperlink and/or URL to the original metadata page. The content must not be changed in any way. Full items must not be sold commercially in any format or medium without formal permission of the copyright holder. The full policy is available online: <http://nrl.northumbria.ac.uk/policies.html>

This document may differ from the final, published version of the research and has been made available online in accordance with publisher policies. To read and/or cite from the published version of the research, please visit the publisher's website (a subscription may be required.)



**Northumbria
University**
NEWCASTLE



UniversityLibrary



OPEN

CMOS-compatible 2-bit optical spectral quantization scheme using a silicon-nanocrystal-based horizontal slot waveguide

SUBJECT AREAS:

NONLINEAR OPTICS

FIBRE OPTICS AND OPTICAL COMMUNICATIONS

SILICON PHOTONICS

OPTOELECTRONIC DEVICES AND COMPONENTS

Zhe Kang¹, Jinhui Yuan^{1,2}, Xianting Zhang¹, Qiang Wu^{1,4}, Xinzhu Sang¹, Gerald Farrell⁴, Chongxiu Yu¹, Feng Li², Hwa Yaw Tam³ & P. K. A. Wai²

Received

22 August 2014

Accepted

5 November 2014

Published

24 November 2014

Correspondence and requests for materials should be addressed to J.Y. (yuanjinhui81@163.com) or Z.K. (kangtony9999@163.com)

¹State Key Laboratory of Information Photonics and Optical Communications, Beijing University of Posts and Telecommunications, P.O. Box72 (BUPT), Beijing, China, ²Photonics Research Centre, Department of Electronic and Information Engineering, The Hong Kong Polytechnic University, Hung Hom, Kowloon, Hong Kong, ³Photonics Research Centre, Department of Electrical Engineering, The Hong Kong Polytechnic University, Hung Hom, Kowloon, Hong Kong, ⁴Photonics Research Centre, Dublin Institute of Technology, Kevin Street, Dublin, Ireland.

All-optical analog-to-digital converters based on the third-order nonlinear effects in silicon waveguide are a promising candidate to overcome the limitation of electronic devices and are suitable for photonic integration. In this paper, a 2-bit optical spectral quantization scheme for on-chip all-optical analog-to-digital conversion is proposed. The proposed scheme is realized by filtering the broadened and split spectrum induced by the self-phase modulation effect in a silicon horizontal slot waveguide filled with silicon-nanocrystal. Nonlinear coefficient as high as $8708 \text{ W}^{-1}/\text{m}$ is obtained because of the tight mode confinement of the horizontal slot waveguide and the high nonlinear refractive index of the silicon-nanocrystal, which provides the enhanced nonlinear interaction and accordingly low power threshold. The results show that a required input peak power level less than 0.4 W can be achieved, along with the 1.98-bit effective-number-of-bit and Gray code output. The proposed scheme can find important applications in on-chip all-optical digital signal processing systems.

Analog-to-digital converters (ADC) as the key front-end digital processing device have extensive applications in ultra-wide-band systems, such as advanced radar systems, real-time signal monitoring, and ultrahigh-speed optical communication systems. Limited by the inherent aperture jitter and the comparator ambiguity, electrical ADCs cannot meet the demands of ultra-wide-band applications^{1–4}. Benefited from the ultrafast response time and passive operation, all-optical ADCs (AOADC) based on third-order nonlinear effects are a promising candidate to overcome the limitation of electronic devices^{5,6}. In last decade, many quantization schemes have been proposed using the nonlinear effects in highly-nonlinear fibers (HNLFs) and photonic crystal fibers (PCFs). For example, the phase quantization schemes use cross-phase modulation (XPM)^{5,7–10}, the spectral quantization schemes use self-phase modulation (SPM)¹¹, XPM¹², intra-pulse stimulated Raman scattering (ISRS)^{6,13–18}, and supercontinuum (SC)¹⁹. However, because of the weak nonlinear interaction in these SiO₂-based materials, the requirements on the fiber length, pulse width, and pulse power are typically very high. These fiber-based AOADCs therefore cannot meet the demands of miniaturization and photonic integration, which are the inevitable development trend of ADCs. Silicon photonic technology is suitable for photonic integration owing to their compatibility with complementary metal oxide semiconductor (CMOS) process. The optical waves can be confined to sub-micron region by the high refractive index of silicon using the silicon-on-insulator (SOI) technology²⁰. Some SOI-based nonlinear signal processing schemes have been proposed^{21–27} but, to the best of our knowledge, there is still no reports on AOADC. In a SOI-based AOADC, the nonlinear interaction is expected to occur only in the specific waveguide but not in other interconnected devices, which requires that the waveguide should provide stronger nonlinear interaction than conventional silicon strip waveguides. The slot waveguide structure allows for very strong mode confinement in a low index nonlinear material sandwiched between two silicon wires^{28,29}. In particular, the horizontal slot structure has the advantages of much thinner slot thickness and minimized scattering loss when compared to the vertical structure³⁰. For the



embedded nonlinear materials with high nonlinear refractive index, e.g. the organic material PTS ($n_2 = 2.2 \times 10^{-16} \text{ m}^2\text{W}^{-1}$ at 1600 nm), the nonlinear coefficient can reach to more than $2 \times 10^4 \text{ W}^{-1}/\text{m}^{28,30}$. However, the organic materials require non-CMOS processes and strict temperature limitation, which render them not suitable for mass-manufacturing^{31,32}. The material silicon-nanocrystal (Si-nc) embedded in silica (SiO_2) has a high n_2 (about one or two orders of magnitude higher than that of silicon) at telecom wavelengths³³ and is completely CMOS foundry compatible using standard chemical vapor deposition (CVD) methods³¹. Thus Si-nc/ SiO_2 is quite suitable for the proposed horizontal slot waveguide with strong nonlinear interaction.

In this paper, we propose a CMOS-compatible 2-bit optical spectral quantization (OSQ) scheme for the first time by filtering the broadened and split spectrum induced by SPM in a silicon horizontal slot waveguide filled with Si-nc/ SiO_2 . The dimensions of the slot waveguide are optimized to achieve the smallest effective mode area, thus making strong nonlinear interaction possible. The quantization performances are studied numerically. In addition, high quantization resolution of the proposed OSQ scheme is demonstrated.

Results

Principle of operation. The schematic diagram of the proposed OSQ scheme is shown in Fig. 1. The sampled pulses at different peak powers, illustrated in inset (a), are delivered into a specially designed silicon horizontal slot waveguide. When the input peak power increases, the output spectra of the pulses first broaden and then split from the center frequency owing to the SPM effects inside the waveguide. The degree of broadening and splitting is directly proportional to the peak powers of the pulses, which can be used for the mapping between the variations of the peak powers and the spectrum parameters. As shown in inset (b), the spectrum of the pulse with higher power broadens and splits while the one with lower power remains unchanged. An arrayed waveguide grating (AWG) with two proper filtering windows at wavelengths λ_1 and λ_2 is used to slice the spectrum of the output pulses of the

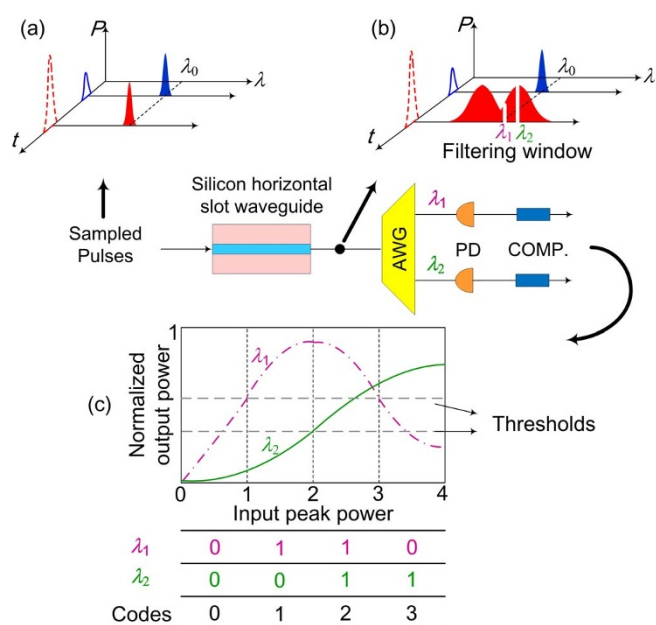


Figure 1 | Schematic diagram of the proposed optical spectral quantization scheme. Inset (a) illustrates two sampled pulses at different peak powers, inset (b) shows the spectrum variations after the silicon horizontal slot waveguide, and inset (c) shows the power transfer functions of the two filtering channels and the available encoding results. AWG: Arrayed waveguide grating, PD: Photodiode, COMP: Comparator.

waveguide. The power transfer functions of the two filtering channels are shown in inset (c). When the input peak power increases, the output power of the λ_1 -channel first increases owing to the spectral broadening and then decreases owing to the spectral splitting. In contrast, the output power of the λ_2 -channel only increases with the input peak power. This is because the wavelength λ_2 , when compared to λ_1 , is farther away from the center wavelength λ_0 so that the filtering range of λ_2 -channel does not contain the spectral splitting region. The output signals of the two filtering channels are then detected by the photodiodes and binary decisions are made by comparators. The available encoding results are shown at the bottom of inset (c), which exhibits a 2-bit Gray code output.

Design of the horizontal slot waveguide. The cross-section of the Si-nc/ SiO_2 -based horizontal slot waveguide is shown in Fig. 2. The lower cladding is a silicon dioxide layer and the upper cladding is air. The slot is filled with Si-nc/ SiO_2 , which is sandwiched between two silicon strip wires and has a thickness s . The upper and lower silicon wires are formed by the amorphous silicon (a-Si) and the crystalline silicon (c-Si), respectively, and have the same height h . The width of the waveguide is w . Since the electric field discontinuity occurs at the horizontal interface for such a waveguide, the quasi transverse-magnetic (TM) polarization should be used for the analysis. The deep-UV lithography method, together with the plasma-enhanced chemical vapor deposition (PECVD) or low-pressure chemical vapor deposition (LPCVD), can be used for the fabrication of such horizontal slot waveguides. The detailed fabrication procedure can be found in³⁴.

In order to obtain the strongest nonlinear interaction inside the waveguide, the minimum effective area (A_{eff}) is investigated with different geometrical parameters. The effective areas at the wavelength of 1.55 μm are calculated for different combinations of w and h when the slot thickness s is increased from 5 to 30 nm. For each given slot thickness, the minimum achievable effective area is found and shown in Fig. 3(a). From Fig. 3(a), the effective area does not vary monotonically with the slot thickness. The minimum value of $A_{\text{eff}} \approx 0.0268 \mu\text{m}^2$ is obtained around $s = 13 \text{ nm}$. Fig. 3(b) shows the optimum geometrical parameters which correspond to the minimum effective area as a function of the slot thickness. We note that the calculated results agree with the results in³⁰.

Based on the results obtained above, the slot thickness of $s = 15 \text{ nm}$ is chosen, which corresponds to $A_{\text{eff}} = 0.027 \mu\text{m}^2$ at 1.55 μm . Accordingly, the width (w) and height (h) are set at 220 and 210 nm respectively. In order to obtain the accurate dispersion properties of the designed horizontal slot waveguide, the material dispersions of a-Si³⁵, c-Si³⁶, Si-nc/ SiO_2 ^{37,38}, and SiO_2 ³⁹ are considered. The calculated transverse profiles of the electric field for quasi-TM polarization at three different wavelengths are shown in Fig. 4. We observed that the electric field is tightly confined inside the slot even for wavelength as long as 1.8 μm . The effective refractive index n_{eff} is

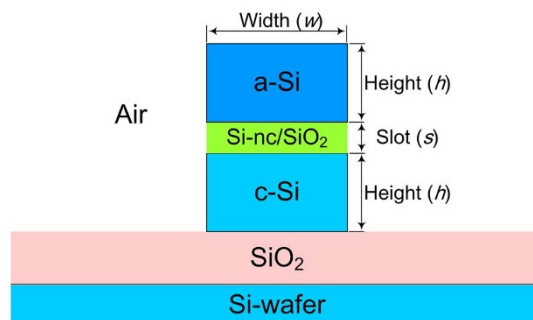


Figure 2 | Cross-section of the Si-nc/ SiO_2 -based horizontal slot waveguide. a-Si: amorphous silicon; c-Si: crystalline silicon.

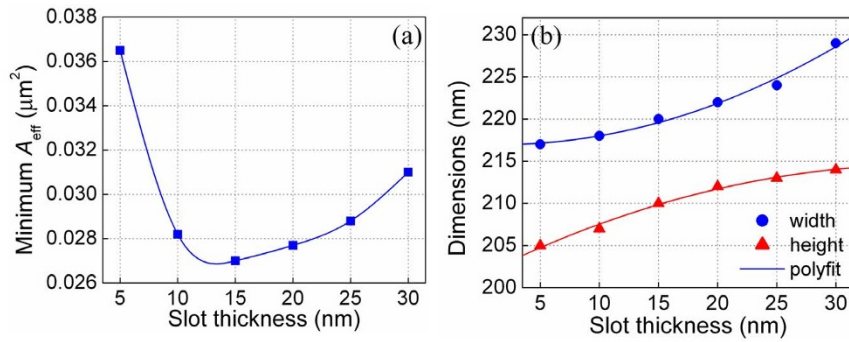


Figure 3 | (a) The minimum achievable effective area as a function of the slot thickness, and (b) the corresponding optimum geometrical parameters as a function of the slot thickness.

calculated and shown in Fig. 5(a). Using the results of n_{eff} we further determined the group index, second- and third-order dispersion parameters, as shown in Figs. 5(a) and 5(b). The designed waveguide has two zero dispersion wavelengths around 1.38 and 1.51 μm , which results in about 130 nm anomalous dispersion regime. The second- (β_2) and third-order (β_3) dispersion coefficients at 1.55 μm are 1.418 ps^2/m and $-0.064 \text{ ps}^3/\text{m}$, respectively.

Quantization performance. The dynamic of an optical pulse inside a silicon waveguide is governed by the modified generalized nonlinear Schrödinger equation (GNLSE), which includes the effects of two-photo absorption (TPA), free-carrier absorption (FCA), and free-carrier dispersion (FCD). The GNLSE is given by

$$\frac{\partial A}{\partial z} = i \sum_{m=2}^{\infty} \frac{i^m \beta_m}{m!} \frac{\partial^m A}{\partial t^m} + i(\gamma_0 + i\gamma_{\text{TPA}}) \left(1 + \frac{i}{\omega_0} \frac{\partial}{\partial t} \right) A(z, t) \times \int_{-\infty}^t R(t-t') |A(z, t')|^2 dt' - \frac{1}{2} (\alpha_l + \alpha_{\text{FCA}}) A + i \frac{\omega_0}{c} n_{\text{FCD}} A \quad (1)$$

where $A(z, t)$ is the slowly varying envelope of the electric field along the propagation direction z , β_m is the m -th dispersion coefficient, ω_0 is the center angular frequency of the optical field, γ_0 and γ_{TPA} are the real and imaginary part of the complex nonlinear coefficient, α_l is the linear loss of the waveguide, α_{FCA} and n_{FCD} are the coefficients of FCA-induced absorption and FCD-induced index change, which are given by $\alpha_{\text{FCA}} = 1.45 \times 10^{-21} (\lambda_0/\lambda_{\text{ref}})^2 N_c$ and $n_{\text{FCD}} = -5.3 \times 10^{-27} (\lambda_0/\lambda_{\text{ref}})^2 N_c$ ²⁰. Here, λ_0 is the input center wavelength, $\lambda_{\text{ref}} = 1.55 \mu\text{m}$ is the reference wavelength, and $N_c(z, t)$ is the free-carrier density defined by

$$\frac{\partial N_c}{\partial t} = \frac{\beta_{\text{TPA}} |A(z, t)|^4}{2hf_0 A_{\text{eff}}^2} - \frac{N_c}{\tau} \quad (2)$$

where β_{TPA} is the TPA parameter, h is the Planck constant, $f_0 = \omega_0/2\pi$ is the center frequency, τ is the effective carrier lifetime that estimated to be about 100 μs ³³.

The Si-nc/SiO₂ used in the simulation is assumed to be with 8% silicon excess, deposited by PECVD method and annealed at 800°C. The Si-nc/SiO₂ has the achievable $\alpha_l = 4.6 \text{ dB}/\text{cm}$ ⁴⁰, $n_2 = 5.8 \times 10^{-4} \text{ cm}^2/\text{GW}$, and $\beta_{\text{TPA}} = 5 \text{ cm}/\text{GW}$ ³³. Using the available A_{eff} of

0.027 μm^2 , the parameter values of $\gamma_0 = 2\pi n_2/\lambda_0 A_{\text{eff}} = 8708 \text{ W}^{-1}/\text{m}$ and $\gamma_{\text{TPA}} = \beta_{\text{TPA}}/2A_{\text{eff}} = 926 \text{ W}^{-1}/\text{m}$ can be obtained.

The nonlinear response function $R(t)$ in Eq. (1) is related to the Raman contribution and is given by $R(t) = (1 - f_R)\delta(t) + f_R h_R(t)$. The Raman response function $h_R(t)$ can be deduced from the Raman response spectrum. The Fourier transform $H_R(\Omega)$ of $h_R(t)$ with a Lorentzian shape is defined by²⁰

$$H_R(\Omega) = \frac{\Omega_R^2}{\Omega_R^2 - \Omega^2 - 2i\Gamma_R\Omega} \quad (3)$$

where $\Omega_R/2\pi = 15.6 \text{ THz}$ is the Raman shift, $\Gamma_R/\pi \approx 105 \text{ GHz}$ is the bandwidth of Raman gain spectrum at room temperature. The parameter f_R is the fractional contribution of the nuclei to the total nonlinear polarization, and $f_R = 0.043$ is obtained by using the normalization condition of $\int_0^{\infty} h_R(t) dt = 1$.

The split-step Fourier method is used to numerically solve Eqs. (1) and (2). A hyperbolic secant pulse source centered at 1.55 μm with 1.2 ps pulse width is utilized. The length of the designed waveguide is 8 mm. The peak power of the pulse is adjusted to simulate the sampled pulses. Fig. 6(a) shows the spectral dynamic of the output pulse of the waveguide when the peak power is increased from 0 to 0.4 W. The spectrum begins to broaden around 0.1 W and splits at 0.2 W. In order to investigate the influences of TPA and FCA, the spectral dynamic without the FCA or TPA effects are shown in Figs. 6(b) and 6(c). We observe that FCA has little effect on the spectral broadening, but TPA significantly limits the spectral broadening. The effect of FCD is negligible because of its low magnitude of 10^{-4} . The spectral profile shows two splitting gaps when TPA is neglected (Fig. 6(c)), but is limited to only one splitting gap with TPA (Figs. 6(a) and 6(b)). Fig. 6(d) shows the 2-D spectral profiles with peak power of 0.4 W at different nonlinear conditions. The FCA effect affects the spectral broadening slightly but reduces the depth of the spectral splitting by about 15 dB. Owing to the moderate peak power used in our simulation, the FCA-induced spectrum asymmetry is not observed, but the TPA-induced decrease in spectral broadening is about 4 nm.

To simultaneously show the temporal and spectral dynamic, the cross-correlation frequency-resolved optical gating (X-FROG) traces

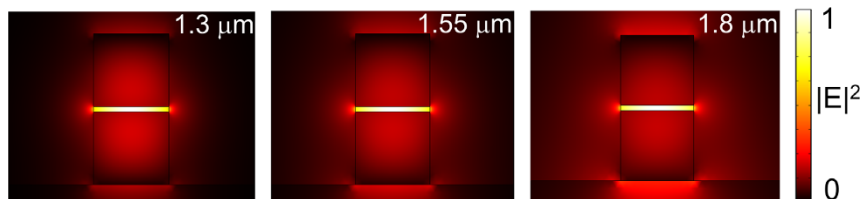


Figure 4 | Transverse profiles of the electric field for quasi-TM polarization at 1.3, 1.5, and 1.8 μm .

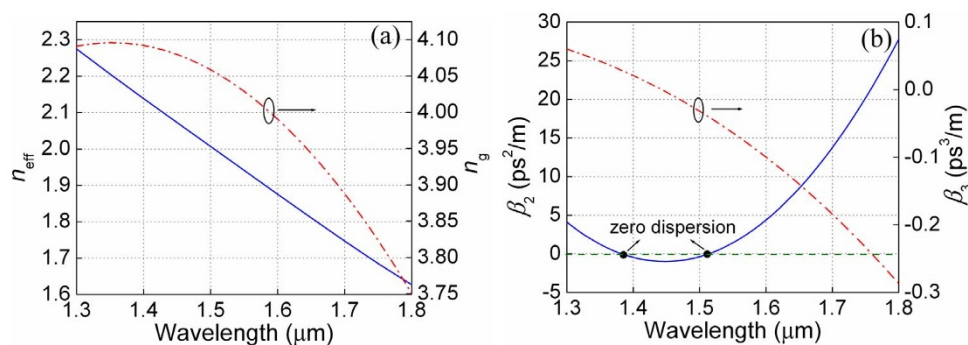


Figure 5 | (a) The effective refractive index and group index, and (b) second- and third-order dispersion coefficients as a function of wavelength.

of the output pulses with peak powers of 0.1, 0.2, 0.3, and 0.4 W are illustrated in Fig. 7. Unlike the obvious broadening and splitting of the spectrum, the temporal profiles of the pulses are only slightly broadened even at peak power of 0.4 W. This is because the dispersion length $L_D = T_0^2/|\beta_2| = 0.33$ m is about 40 times larger than the waveguide length of 8 mm, which means chromatic dispersion basically does not affect the pulse dynamic. By contrast, the nonlinear length is $L_{\text{NL}} = 1/\gamma_0 P_0 = 0.3$ mm, thus the pulse evolution dynamic is dominated by the nonlinear interaction.

The output signal of the waveguide is delivered into an AWG with two filtering channels, Channel-1 and Channel-2. The frequency transfer functions of the two filtering channels are both 6-order Chebyshev type, which have the stop-band extinction of 34 dB and the pass-band amplitude ripple of 0.5 dB. In order to find the optimum filtering windows, we investigate the variation of the power transfer function of the filter by increasing the center wavelength from 1550.8 to 1553.2 nm with 0.2 nm filtering bandwidth. As shown in Fig. 8(a), the peak of the transfer function shifts towards higher input power when the center wavelength increases. It should be noted that two requirements must be met to obtain a uniform quantization step length. For Channel-1, since the maximum input peak power is 0.4 W, the filtered powers at the input peak powers of

0.1 and 0.3 W must be identical to ensure that the lengths of the first and fourth quantization steps are both 0.1. For Channel-2, the filtered power at 0.2 W input should be lower than the case of the 0.4 W input. Thus, the filtered power at 0.2 W input can be used as the decision threshold to obtain two quantization steps with uniform length of 0.2. When both requirements are satisfied, four quantization steps with same length of 0.1 can be obtained. The requirement of the Channel-2 can be satisfied with the center wavelength larger than 1551.6 nm. For Channel-1, the optimum center wavelength is found to be 1551.2 nm. It is desired that the thresholds of the two channels are the same in order to reduce the complexity of the ADC. This can be achieved by setting the center wavelength of the Channel-2 at 1552.9 nm.

We then investigate the influence of the filtering bandwidth by varying the bandwidth from 0.2 to 1.2 nm at the two optimum center wavelengths of 1551.2 and 1552.9 nm, as shown in Fig. 8(b). It is evident that the power transfer function of the Channel-1 changes slightly with the bandwidth, and the transfer function of the Channel-2 remains almost unchanged.

Fig. 9(a) shows the power transfer functions of the two quantization channels at the optimum center wavelengths with the filtering bandwidth of 0.2 nm. The transmitted powers of the Channel-1 at

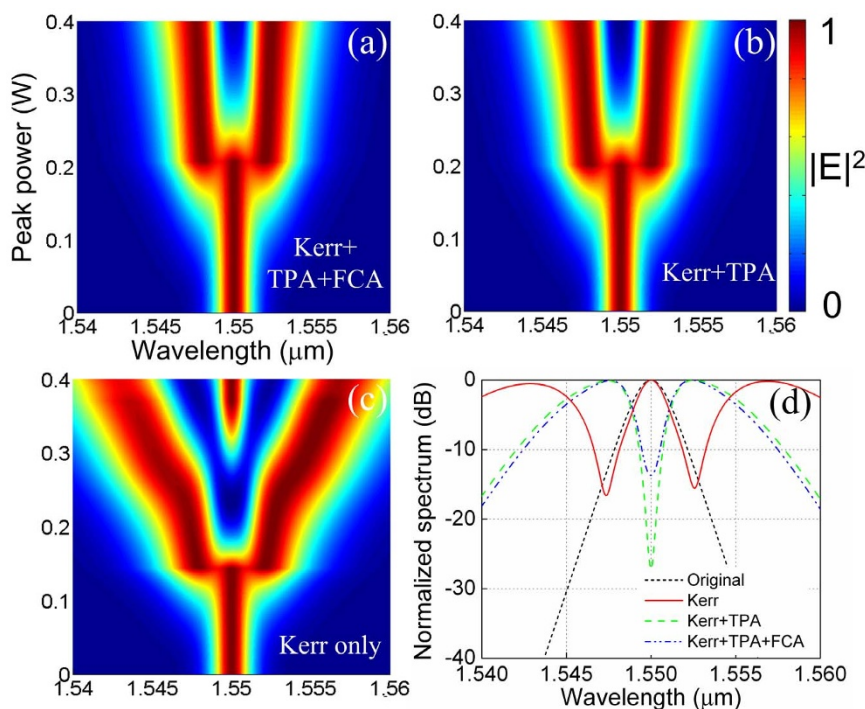


Figure 6 | The spectral dynamic of the output pulse of the waveguide as a function of the input peak power with the (a) Kerr, TPA, and FCA effects, (b) Kerr and TPA effects, and (c) Kerr effect only. (d) 2-D spectral profiles at peak power of 0.4 W for different nonlinear conditions.

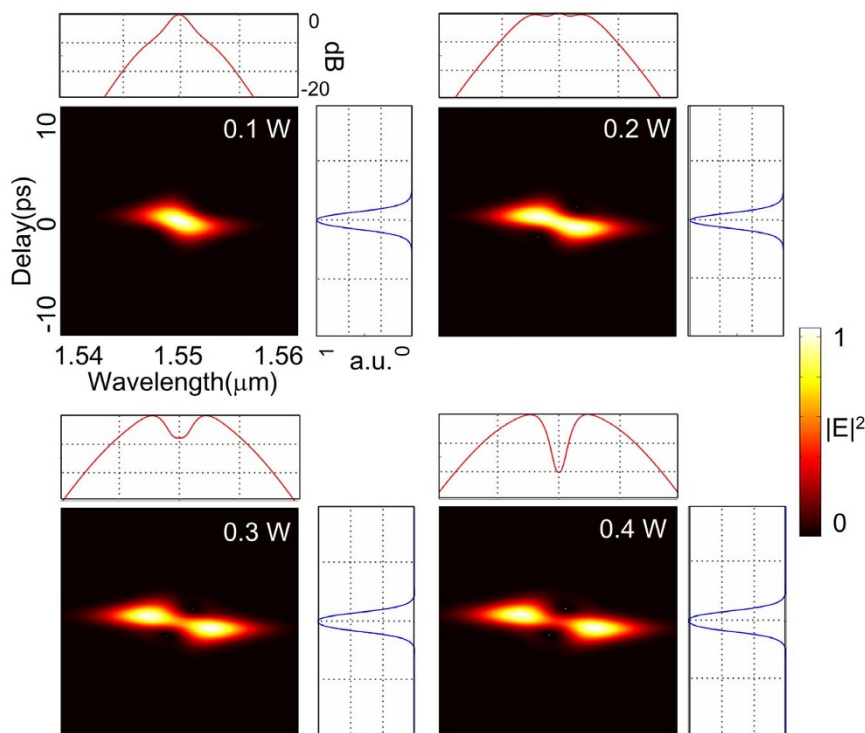


Figure 7 | X-FROG traces of the output pulse of the waveguide with different input peak powers. The corresponding normalized temporal (blue line) and spectral (red line) profiles are also illustrated.

0.1 and 0.3 W input peak power are both $3.66 \mu\text{W}$, which is only $0.02 \mu\text{W}$ larger than the required decision power of the Channel-2. This small difference allows the same decision threshold to be used with only slight degradation of quantization resolution. Fig. 9(b) shows the quantization transfer function of the proposed 2-bit quantizer for the decision threshold of $3.66 \mu\text{W}$. The simulated transfer function is found to be very similar to that of the ideal ADC. The inset of Fig. 9(b) shows the tiny difference between the two transfer functions. Assuming the analog input is a sinusoidal wave, the effective-number-of-bit (ENOB) can be calculated by^{1,9}

$$ENOB = \frac{SNR - 1.76}{6.02} \quad (4)$$

$$SNR = 10 \log_{10} \left(\frac{RMS_power}{RMS_noise} \right) = 10 \log_{10} \left\{ \frac{[P_{FS}/2\sqrt{2}]^2}{\frac{1}{P_{FS}} \left[\int_0^{\Delta} p^2 dp + \sum_{i=1}^{2^B-1} \left(\int_0^{\Delta/2+\Delta_i} p^2 dp + \int_{\Delta/2+\Delta_i}^{\Delta} (p-\Delta)^2 dp \right) \right]} \right\} \quad (5)$$

where SNR is the signal-to-noise ratio, RMS_power and RMS_noise are the root-mean-square of the power and the quantization errors, P_{FS} is the full-scale of power range, $\Delta = P_{FS}/2^B$ is the power of the least significant bit (LSB), B is the ideal number of bit, and Δ_i is the nonlinear error of the i -th quantization step. The SNR is calculated to be 13.68 dB, thus the ENOB is 1.98-bit.

The AWG can also be realized by silicon devices, e.g. silicon ring resonators^{3,41}, which will ensure CMOS-compatibility of the proposed quantizer. The required bandwidth of 0.2 nm and center wavelengths of 1551.2 and 1552.9 nm are achievable by appropriate design of the ring resonators³. It is expected that optical pulses with less than 0.4 W peak power do not have nonlinear interaction inside the AWG so that the quantization performances would not be degraded. The silicon ring resonators based filters are typically formed by silicon strip nanowires. For such silicon strip waveguide, the achievable minimum effective area is found to be about $0.05 \mu\text{m}^2$

with both the length and height of the strip waveguide within the range of $200 \sim 400 \text{ nm}$ ²⁸. Using the same parameters as the above except that $n_2 = 6 \times 10^{-5} \text{ cm}^2/\text{GW}$, $\beta_{\text{TPA}} = 0.5 \text{ cm}/\text{GW}$ ⁴², and $A_{\text{eff}} = 0.05 \mu\text{m}^2$, the spectral dynamic of the optical pulses with different input peak powers are simulated and shown in Fig. 10. It is evident the spectrum remains almost unchanged when the peak power is less than 0.4 W and only slightly broadened even at 4 W. This is because the nonlinear coefficient of such strip nanowires is only $486 \text{ W}^{-1}/\text{m}$, which is about 18 times less than that of the proposed slot waveguide. The nonlinear interaction length at 0.4 W peak power for such silicon nanowires is found to be 5.1 mm, which is very close to the waveguide length 8 mm, thus the nonlinear accumulation is small. The nonlinear effects in such silicon nanowires are negligible when the input peak power is less than 0.4 W. It is therefore feasible to combine the proposed quantizer with other silicon nanowires based functional devices.

Discussion

Owing to the inherent limitation of spectral broadening, it is difficult for the proposed OSQ to realize more than 2-bit quantization. However, as discussed above, since the proposed OSQ requires low power threshold, it is possible to combine the proposed OSQ with other existing quantization schemes that use linear modulation, e.g. phase-shifted optical quantization (PSOQ). The combination can be realized via a cascaded optical quantization (COQ) structure, as shown in Fig. 11.

The COQ structure is composed of two cascaded quantization stages. The first-stage quantization, which can be realized by the unbalanced Mach-Zehnder modulator (UMZM) proposed in^{43,44}, implements the N -channel PSOQ and generates N different sinusoidal power transfer functions corresponding to the different channels. Such a PSOQ scheme can provide a resolution of $\log_2(2N)$ -bit^{44,45}. The inset (a) shows the power transfer functions and the coding results of the first-stage quantization in the case of two channels ($N = 2$). A 2-bit resolution is obtained. Instead of direct detection and binary decision, the proposed 2-bit OSQ is used to

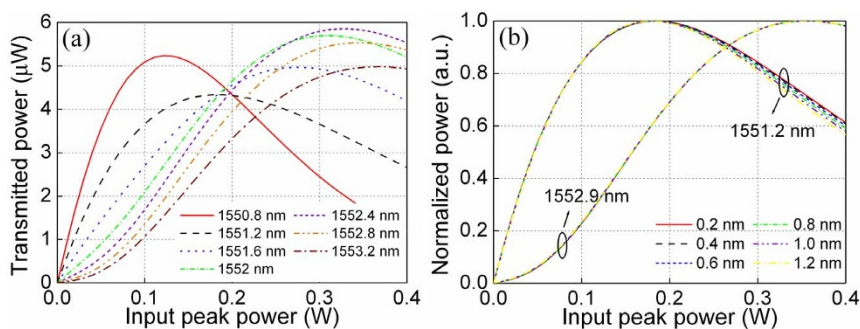


Figure 8 | (a) Power transfer functions of the filter with center wavelengths from 1550.8 to 1553.2 nm and the filtering bandwidth of 0.2 nm. (b) Power transfer functions of the two quantization channels at the optimum center wavelengths of 1551.2 and 1552.9 nm with filtering bandwidth varying from 0.2 to 1.2 nm.

further quantize the output power of the first-stage quantization module. With the second-stage quantization, the number of quantization level increases from 4 to 12 without adding additional channels, as shown in the inset (b). The total resolution is then enhanced to $\log_2[2N(2^2 - 1)] = 3.59$ -bit, which is 1.59-bit higher than individual PSOQ and OSQ. In the case of $N = 16$, a competitive 6.59-bit resolution can be achieved. Besides resolution enhancement, such a COQ-ADC can also provide high analog bandwidth because of the all-optical process in both quantization stages. Since the UMZM can also be fabricated by silicon photonics technology⁴⁶, the entire components of the COQ-ADC is CMOS-compatible.

Coupling loss is a key factor to be considered for practical implementation of silicon-based functional devices. There are two types of coupling loss in the proposed device: fiber-to-waveguide and waveguide-to-waveguide. The former only occurs between the transmitter part and the functional waveguide. High coupling efficiency of 93% (0.3 dB loss) at 1550 nm has been numerically obtained using the inverted taper approach and lensed fibers⁴⁷. To ensure the required power threshold of 0.4 W is attained, the peak power of the transmitter part should reach to at least 0.43 W. Considering a pulse width of 1.2 ps at pulse repetition rate of 10 GHz, the average power is only 5.2 mW. Such a power level is moderate and achievable. Another main fiber-to-waveguide coupling approach is based on grating couplers. A coupling efficiency of 20% (7 dB loss) at 1550 nm has been achieved experimentally in⁴⁸, which requires that the peak power of the transmitter part reaches 2 W, i.e. an average power of 24 mW. We note that pulsed sources at peak power of several Watts and pulse width of several picoseconds are achievable even at high repetition rates of tens of GHz⁴⁹. For higher peak powers, the pulsed sources can be integrated on a separate chip³ together with semiconductor optical amplifiers. The discussion above aims at the coupling between fiber and silicon slot waveguide. For the

case of fiber to silicon strip waveguide, the low coupling loss of 0.36 dB is obtained experimentally⁵⁰. The impact of fiber-to-waveguide coupling loss is therefore negligible.

In contrast, the waveguide-to-waveguide coupling loss that exists in optical interconnections will determine the feasibility of the proposed device. This is because the proposed 2-bit quantizer may be joint indirectly with the transmitter part through interconnecting with other linear functional devices which can be realized by silicon strip waveguides. If the interconnection loss is very large, the high power inside the linear devices can induce undesired nonlinear effects, which could severely degrade the quantization performance. However, we note that ultralow loss of <0.1 dB strip-to-slot mode converter at the telecom waveband has been reported in experiment⁵¹, which is based on the logarithmically tapering approach. Considering the propagation loss of a strip waveguide to be typically around 2 dB/cm⁵¹, the peak power inside a strip waveguide several millimeters long can be less than 0.6 W. It is unlikely that such a moderate peak power will lead to any undesired nonlinear effects in the linear devices from the results shown in Fig. 10. Taking the proposed COQ-ADC as an example, an UMZM could interconnect between the 2-bit quantizer and the transmitter. A similar silicon-based structure reported in⁴⁶ can be used to realize such an UMZM, which exhibits a total loss of 6 dB where the coupling loss is 4 dB and the propagation loss is 2 dB. Combined with the 0.1 dB strip-to-slot coupling loss, the peak power inside the UMZM and at the transmitter part are expected to be about 0.6 and 1.6 W, respectively, which correspond to average power of only 7.2 and 19.2 mW for repetition rate at 10 GHz and pulse width at 1.2 ps. Both of the power requirements can easily be satisfied. We therefore conclude that using the existing efficient waveguide coupling techniques and the moderate peak power threshold we obtained, the problem of coupling loss is unlikely to affect negatively the feasibility of the proposed scheme.

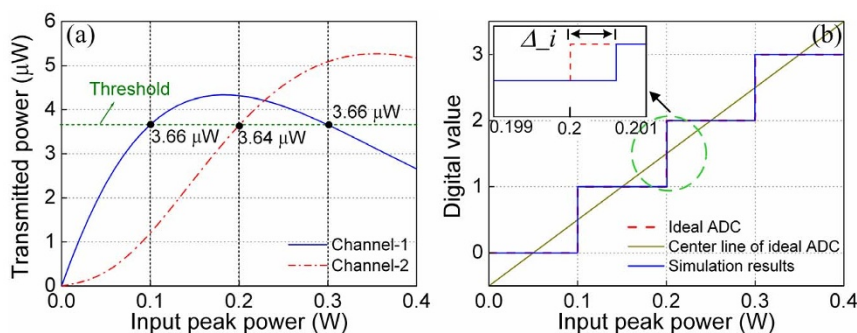


Figure 9 | (a) Power transfer functions of the two quantization channels at the center wavelengths of 1551.2 and 1552.9 nm. The filtering bandwidth is 0.2 nm. (b) Quantization transfer function of the proposed 2-bit quantizer. Inset: the zoom-in view.

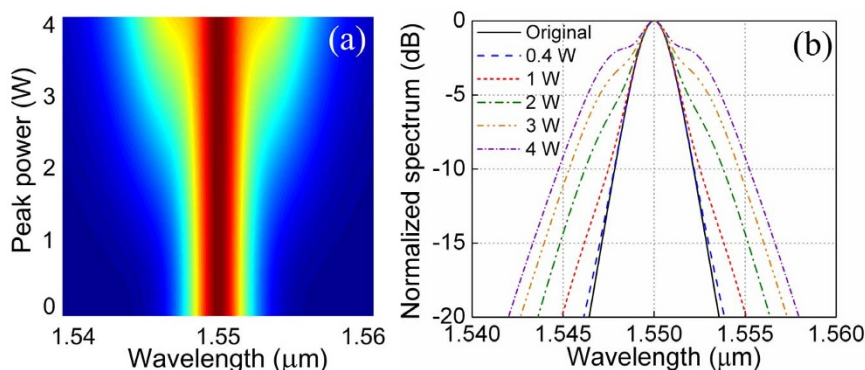


Figure 10 | (a) Spectral dynamic of the optical field with the input peak power at the end of a silicon nanowire with effective area of $0.05 \mu\text{m}^2$, and (b) the corresponding 2-D spectral profiles.

In summary, we propose a CMOS-compatible 2-bit OSQ scheme by filtering the broadened and split spectrum induced by SPM in a silicon horizontal slot waveguide filled with Si-nc/SiO₂. By optimizing the dimensions of the slot waveguide, the nonlinear coefficient of $8708 \text{ W}^{-1}/\text{m}$ can be obtained, which gives a strong Kerr nonlinear interaction and low power threshold. Using simulation, we show that the proposed 2-bit quantization can be realized with an ENOB of 1.98-bit and the required peak power is less than 0.4 W. Thus the requirement on the optical sources is reduced, and the interconnection between the proposed nonlinear OSQ and other silicon-based functional devices is possible. We also propose to combine the 2-bit OSQ with a conventional PSOQ via COQ structure in order to achieve higher quantization resolution. We show that resolution up to 6-bit can be obtained with such a COQ-ADC. Because of the moderate power threshold and achievable ultralow loss strip-to-slot mode converters, the proposed COQ-ADC is feasible and can find important applications in the on-chip all-optical digital signal processing systems.

Methods

Search of the minimum effective area and the optimum geometrical parameters. For a high refractive index contrast waveguide, the A_{eff} is defined by^{28,30}

$$A_{\text{eff}} = \frac{Z_0^2 \left| \iint_{D_{\text{total}}} \text{Re} \left[\vec{E}(x,y) \times \vec{H}^*(x,y) \right] \cdot \vec{e}_z dx dy \right|^2}{n_{\text{NL}}^2 \iint_{D_{\text{NL}}} |\vec{E}(x,y)|^4 dx dy} \quad (6)$$

where $Z_0 = 377 \Omega$ is the free space wave impedance, n_{NL} the refractive index of the nonlinear material filled in the slot, $\vec{E}(x,y)$ the vector electric, and $\vec{H}(x,y)$ the vector magnetic field profiles of the TM-like mode. The upper integral covers the whole cross-section D_{total} , whereas the lower integral considers only within the slot region D_{NL} .

A full-vector finite element method (FEM) based mode solver is used for the eigenmode calculations. The simulation domain is $4 \times 4 \mu\text{m}^2$ with a $0.4 \mu\text{m}$ thick perfectly matched layer. An adaptive mesh refinement is used to ensure the accuracy of the calculations. In order to determine the optimum geometrical parameters for the minimum effective area, we adopt the following procedure. Firstly, a cross grid of width (w) and height (h) is defined with $w, h \in \{200 \text{ nm}, 205 \text{ nm}, \dots, 230 \text{ nm}\}$. The region is chosen with reference to the results in³⁰. Secondly, when the slot thickness is increased from 5 to 30 nm, the effective areas are calculated at wavelength $1.55 \mu\text{m}$ for different combinations of w and h . Finally, at each given slot thickness, if the statistics of the calculated effective areas has an inflection point which corresponds to the minimum value, the value is recorded as the minimum effective area and the corresponding w and h are the optimum geometrical parameters. If such an inflection point is not found, we extend the boundary values of w and h , and repeat the above procedure until the minimum effective area is found.

Model of the X-FROG trace. The X-FROG trace obtained in our simulation is based on the difference-frequency generation XFROG algorithm, which is given by⁵²

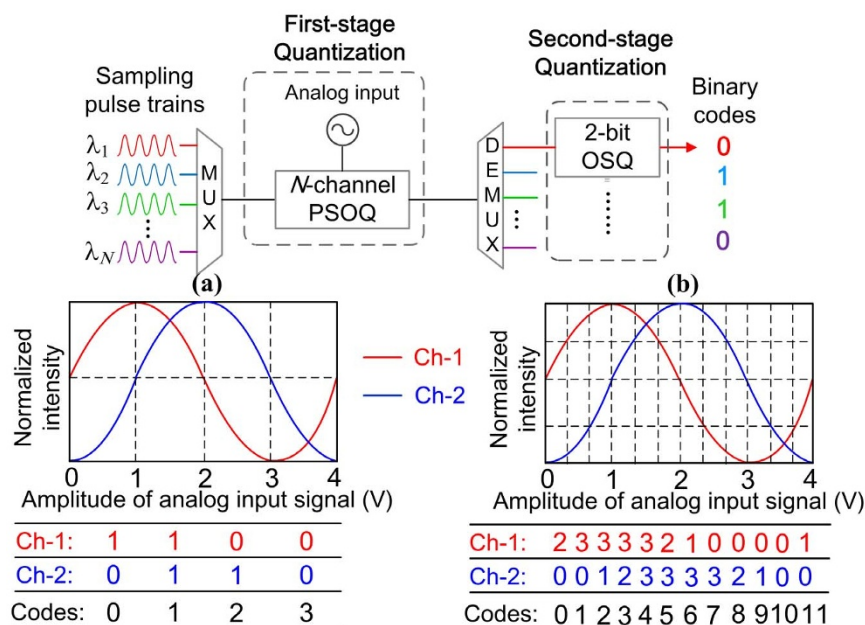


Figure 11 | Schematic diagram of the proposed COQ-ADC. Inset (a) illustrates the power transfer functions and coding results of the first-stage quantization for two channels ($N = 2$), and inset (b) illustrates the combined power transfer functions and coding results of the two quantization stages. PSOQ: phase-shifted optical quantization; OSQ: optical spectral quantization; MUX: multiplexer; DEMUX: demultiplexer.



$$I_{XFRQG}(\omega, \tau) = \left| \int_{-\infty}^{\infty} E_{\text{sig}}(t) \cdot E_{\text{ref}}^*(t - \tau) \exp(-j\omega t) dt \right|^2 \quad (7)$$

Where $E_{\text{sig}}(t)$ is the electric field of the measured signal, $E_{\text{ref}}^*(t - \tau)$ is the conjugate electric field of the reference signal delayed by time τ . The reference signal is characterized by the initial input signal.

1. Walden, R. H. Analog-to-digital converter survey and analysis. *IEEE J. Sel. Areas Commun.* **17**, 539–550 (1999).
2. Valley, G. C. Photonic analog-to-digital converters. *Opt. Express* **15**, 1955–1982 (2007).
3. Khilo, A. *et al.* Potonic ADC: overcoming the bottleneck of electronic jitter. *Opt. Express* **20**, 4454–4469 (2012).
4. Han, Y. & Jalali, B. Photonic Time-stretched analog-to-digital converter: fundamental concepts and practical considerations. *J. Lightwave Technol.* **21**, 3085–3103 (2003).
5. Ikeda, K., Abdul, J. M., Namiki, S. & Kitayama, K. I. Optical quantizing and coding for ultrafast A/D conversion using nonlinear fiber-optic switches based on Sagnac interferometer. *Opt. Express* **13**, 4296–4302 (2005).
6. Satoh, T., Takahashi, K., Matsui, H., Itoh, K. & Konishi, T. 10-GS/s 5-bit real-time optical quantization for photonic analog-to-digital conversion. *IEEE Photon. Technol. Lett.* **24**, 830–832 (2012).
7. Ikeda, K. *et al.* Design considerations of all-optical A/D conversion: nonlinear fiber-optic Sagnac-loop interferometer-based optical quantizing and coding. *J. Lightwave Technol.* **24**, 2618–2628 (2006).
8. Miyoshi, Y. *et al.* All-optical analog-to-digital conversion using split-and-delay technique. *J. Lightwave Technol.* **25**, 1339–1347 (2007).
9. Miyoshi, Y., Takagi, S., Namiki, S. & Kitayama, K. I. Multiperiod PM-NOLM with dynamic counter-propagating effects compensation for 5-bit all-optical analog-to-digital conversion and its performance evaluations. *J. Lightwave Technol.* **28**, 415–422 (2010).
10. Miyoshi, Y., Namiki, S. & Kitayama, K. I. Performance evaluation of resolution-enhanced ADC using optical multiperiod transfer functions of NOLMs. *IEEE J. Sel. Topics Quantum Electron.* **18**, 779–784 (2012).
11. Oda, S. & Maruta, A. Two-bit all-optical analog-to-digital conversion by filtering broadened and split spectrum induced by soliton effect or self-phase modulation in fiber. *IEEE J. Sel. Topics Quantum Electron.* **12**, 307–314 (2006).
12. Ho, P. P., Wang, Q. Z., Chen, J., Liu, Q. D. & Alfano, R. R. Ultrafast optical pulse digitization with unary spectrally encoded cross-phase modulation. *Appl. Opt.* **36**, 3425–3429 (1997).
13. Nishitani, T., Konishi, T. & Itoh, K. Optical coding scheme using optical interconnection for high sampling rate and high resolution photonic analog-to-digital conversion. *Opt. Express* **15**, 15812–15817 (2007).
14. Nishitani, T., Konishi, T. & Itoh, K. Resolution improvement of all-optical analog-to-digital conversion employing self-frequency shift and self-phase-modulation-induced spectral compression. *IEEE J. Sel. Topics Quantum Electron.* **14**, 724–732 (2008).
15. Konishi, T., Takahashi, K., Matsui, H., Satoh, T. & Itoh, K. Five-bit parallel operation of optical quantization and coding for photonic analog-to-digital conversion. *Opt. Express* **19**, 16106–16114 (2011).
16. Takahashi, K., Matsui, H., Nagashima, T. & Konishi, T. Resolution upgrade toward 6-bit optical quantization using power-to-wavelength conversion for photonic analog-to-digital conversion. *Opt. Lett.* **38**, 4864–4867 (2013).
17. Kang, Z. *et al.* Lumped time-delay compensation scheme for coding synchronization in the nonlinear spectral quantization-based all-optical analog-to-digital conversion. *IEEE Photon. J.* **5**, 7201109(1–9) (2013).
18. Kang, Z. *et al.* Six-bit all-optical quantization using photonic crystal fiber with soliton self-frequency shift and pre-chirp spectral compression techniques. *Chin. Phys. B* **22**, 114211(1–5) (2013).
19. Oda, S. & Maruta, A. A novel quantization scheme by slicing supercontinuum spectrum for all-optical analog-to-digital conversion. *IEEE Photon. Technol. Lett.* **17**, 465–467 (2005).
20. Lin, Q., Painter, O. J. & Agrawal, G. P. Nonlinear optical phenomena in silicon waveguides: Modeling and applications. *Opt. Express* **15**, 16604–16644 (2007).
21. Boyraz, O. & Jalali, B. Demonstration of a silicon Raman laser. *Opt. Express* **12**, 5269–5273 (2004).
22. Liu, A. *et al.* High-speed optical modulation based on carrier depletion in a silicon waveguide. *Opt. Express* **15**, 660–668 (2007).
23. Foster, M. A., Turner, A. C., Salem, R., Lipson, M. & Gaeta, A. L. Broad-band continuous-wave parametric wavelength conversion in silicon nanowaveguides. *Opt. Express* **15**, 12949–12958 (2007).
24. Almeida, V. R., Barrios, C. A., Panepucci, R. R. & Lipson, M. All-optical control of light on a silicon chip. *Nature* **431**, 1081–1084 (2004).
25. Salem, R. *et al.* Signal regeneration using low-power four-wave mixing on silicon chip. *Nat. Photonics* **2**, 35–38 (2008).
26. Boyraz, O. Nanoscale signal regeneration. *Nat. Photonics* **2**, 12–13 (2008).
27. Sang, X. Z. & Boyraz, O. Gain and noise characteristics of high-bit-rate silicon parametric amplifiers. *Opt. Express* **16**, 13122–13132 (2008).

28. Koos, C., Jacome, L., Poulton, C., Leuthold, J. & Freude, W. Nonlinear silicon-on-insulator waveguides for all-optical signal processing. *Opt. Express* **15**, 5976–5990 (2007).
29. Koos, C. *et al.* All-optical high-speed signal processing with silicon-organic hybrid slot waveguides. *Nat. Photonics* **3**, 216–219 (2009).
30. Mueller, P., Wellenzohn, M. & Hainberger, R. Nonlinearity of optimized silicon photonic slot waveguides. *Opt. Express* **17**, 9282–9287 (2009).
31. Martinez, A. *et al.* Ultrafast all-optical switching in a silicon-nanocrystal-based silicon slot. *Nano Lett.* **10**, 1506–1511 (2010).
32. Matres, J. *et al.* Low TPA and free-carrier effects in silicon nanocrystal-based horizontal slot waveguides. *Opt. Express* **20**, 23838–23845 (2012).
33. Spano, R. *et al.* Bound electronic and free carrier nonlinearities in Silicon nanocrystals at 1550 nm. *Opt. Express* **17**, 3941–3950 (2009).
34. Jordana, E. *et al.* Deep-UV lithography fabrication of slot waveguides and sandwiched waveguides for nonlinear applications. *IEEE International Conference on Group IV Photonics*, (Institute of Electrical and Electronics Engineers, 2007), paper WB4.
35. Polyanskiy, M. N. Refractive index database. (2008) Date of access: 30/02/2084. <http://refractiveindex.info>.
36. Yin, L. H., Lin, Q. & Agrawal, G. P. Soliton fission and supercontinuum generation in silicon waveguides. *Opt. Lett.* **32**, 391–393 (2007).
37. Hernández, S. *et al.* Linear and nonlinear optical properties of Si nanocrystals in SiO₂ deposited by plasma-enhanced chemical-vapor deposition. *J. Appl. Phys.* **103**, 064309(1–6) (2008).
38. Zhang, L. *et al.* Flat and low dispersion in highly nonlinear slot waveguides. *Opt. Express* **18**, 13187–13193 (2010).
39. Agrawal, G. P. *Nonlinear Fiber Optics* (Academic Press, San Diego, 2001).
40. Guider, R. *et al.* NanoSi low loss horizontal slot waveguides coupled to high Q ring resonators. *Opt. Express* **17**, 20762–20770 (2009).
41. Dong, P. *et al.* GHz-bandwidth optical filters based on high-order silicon ring resonators. *Opt. Express* **18**, 23784–23789 (2010).
42. Bristow, A. D., Rotenberg, N. & Van Driel, H. M. Two-photon absorption and Kerr coefficients of silicon for 850–2200 nm. *Appl. Phys. Lett.* **90**, 191104(1–3) (2007).
43. Kang, Z. *et al.* Resolution-enhanced all-optical analog-to-digital converter employing cascade optical quantization operation. *Opt. Express* **22**, 21441–21453 (2014).
44. Sarantos, C. H. & Dagli, N. A photonic analog-to-digital converter based on an unbalanced Mach-Zehnder quantizer. *Opt. Express* **18**, 14598–14603 (2010).
45. Wang, Y., Zhang, H. M., Wu, Q. W. & Yao, M. Y. Improvement of photonic ADC based on phase-shifted optical quantization by using additional modulators. *IEEE Photon. Technol. Lett.* **24**, 566–568 (2012).
46. Ziebell, M. *et al.* 40 Gbit/s low-loss silicon optical modulator based on a pipin diode. *Opt. Express* **20**, 10591–10596 (2012).
47. Galan, J. V., Sanchis, P., Blasco, J., Martinez, A. & Marti, J. High efficiency fiber coupling to silicon sandwiched slot waveguides. *Opt. Commun.* **281**, 5173–5176 (2008).
48. Galan, J. V. *et al.* Silicon sandwiched slot waveguide grating couplers. *Electron. Lett.* **45**, 20093138(1–2) (2009).
49. Lecomte, S. *et al.* Diode-pumped passively mode-locked Nd:YVO₄ lasers with 40-GHz repetition rate. *IEEE J. Quantum Electron.* **41**, 45–52 (2005).
50. Pu, M. H., Liu, L., Ou, H. Y., Yvind, K. & Hvam, J. M. Ultra-low-loss inverted taper coupler for silicon-on-insulator ridge waveguide. *Opt. Commun.* **283**, 3678–3682 (2010).
51. Palmer, R. *et al.* Low-loss silicon strip-to-slot mode converters. *IEEE Photon. J.* **5**, 2200409(1–10) (2013).
52. Linden, S., Kuhl, J. & Giessen, H. Amplitude and phase characterization of weak blue ultrashort pulses by downconversion. *Opt. Lett.* **24**, 569–571 (1999).

Acknowledgments

This work was supported in part by the National Basic Research Program under Grant 2010CB327601, the National Natural Science Foundation of China under Grants 61475023, 61307109, and 61475131, the Natural Science Foundation of Beijing under Grant 4152037, the National High-Technology Research and Development Program of China under Grant 2013AA031501, the Specialized Research Fund for the Doctoral Program of Higher Education under Grant 20120005120021, the Fundamental Research Funds for the Central Universities under Grant 2013RC1202, the Program for New Century Excellent Talents in University under Grant NECT-11-0596, the Beijing Nova Program under Grant 2011066, the Fund of State Key Laboratory of Information Photonics and Optical Communications (BUPT) P. R. China, the Hong Kong Scholars Program 2013 under Grant PolyU G-YZ45, and the Science Foundation Ireland (SFI) under Grants SFI/12/ISCA/2496 and SFI/13/ISCA/2845.

Author contributions

K.Z. and Y.J.H. designed the research. Z.X.T. and L.F. prepared figures 1–3, W.Q. carried out the mode analysis and prepared figure 4. K.Z., Y.J.H. and S.X.Z. carried out the simulation of nonlinear pulse propagation under the supervision of F.G., C.X.Y. and W.P.K.A. T.H.Y. prepared figure 7. K.Z., Y.J.H. and W.P.K.A. wrote the main manuscript. All authors contributed to revision of the manuscript.



Additional information

Competing financial interests: The authors declare no competing financial interests.

How to cite this article: Kang, Z. *et al.* CMOS-compatible 2-bit optical spectral quantization scheme using a silicon-nanocrystal-based horizontal slot waveguide. *Sci. Rep.* **4**, 7177; DOI:10.1038/srep07177 (2014).



This work is licensed under a Creative Commons Attribution-NonCommercial-ShareAlike 4.0 International License. The images or other third party material in this article are included in the article's Creative Commons license, unless indicated otherwise in the credit line; if the material is not included under the Creative Commons license, users will need to obtain permission from the license holder in order to reproduce the material. To view a copy of this license, visit <http://creativecommons.org/licenses/by-nc-sa/4.0/>